# Boiling nucleation on melanosomes and microbeads transiently heated by nanosecond and microsecond laser pulses

**Jörg Neumann**
**Ralf Brinkmann**
Medizinisches Laserzentrum Lübeck GmbH
Peter-Monnik-Weg 4
D-23562 Lübeck, Germany
E-mail: neumann@mll.mu-luebeck.de

**Abstract.** Selective tissue damage on the cellular level can be achieved by microbubble formation around laser-heated intracellular pigments. To acquire a more detailed understanding of the laser tissue interaction in the highly pigmented retinal pigment epithelium (RPE), we irradiate aqueous suspensions of absorbing microparticles by short pulsed laser irradiation (12 ns, 240 ns, and 1.8 $\mu$s). Porcine retinal pigment epithelial melanosomes, gold beads, and magnetic silica beads are used as absorbers. Pulsed laser heating of the particles leads to vaporization of the surrounding liquid. The resulting transient microbubbles on the particle surface are imaged directly on a microscopic level by fast flash light photography. Furthermore, the bubble dynamics is probed by a low power laser. Threshold radiant exposures for bubble formation and nucleation temperatures are experimentally determined. Superheating of the surrounding water to 150 °C for melanosomes and to more than 200 °C for magnetic silica beads (∅=3 $\mu$m) and gold beads (∅=500 nm) is achieved. With these data, the absorption coefficient of a melanosome is calculated by thermal modeling of the experimental thresholds for bubble formation.  [DOI: 10.1117/1.1896969]

Keywords: selective photothermolysis; bubble; superheating; melanosome; retinal pigment epithelium; nucleation; time-resolved microscopy.

Paper 04034 received Mar. 12, 2004; revised manuscript received Aug. 12, 2004; accepted for publication Oct. 15, 2004; published online Apr. 22, 2005.

## 1 Introduction

The concept of selective targeting of strongly absorbing structures in weakly absorbing tissues was introduced by Anderson and Parrish.[1] If heat is generated within an absorbing target more rapidly than heat can diffuse away, high temperatures can be obtained, leading to vaporization when applying appropriate energy. The resulting bubbles around laser-heated intracellular pigment particles cause spatial confined mechanical damage to the surrounding tissue.[2]

A prominent example of selective targeting is the retina. The aim of the selective retina treatment[3–5] (SRT) is to selectively damage dysfunctional areas of the retinal pigment epithelium (RPE), which is a monocellular layer heavily loaded with pigment particles, while sparing the adjacent photoreceptors. Due to short pulsed laser exposure, bubbles form around the pigments in the RPE. However, large bubbles might also damage the neighboring photoreceptors causing scotoma.[6] SRT is thought to share the therapeutic benefits from conventional photocoagulation, without affecting the function of the photoreceptors in the irradiated areas and avoiding loss of vision. The commonly used laser pulse duration in clinical SRT is 1.7 $\mu$s.

Other biomedical applications, in which bubble formation around laser-heated microparticles is involved, are proposed for anticancer therapy. Originally unpigmented tumor cells are labeled selectively by bioconjugated light-absorbing exogenous microbeads. Selective destruction of cells, which contain these absorbers, can be triggered due to laser-induced microbubbles.[7–10] Furthermore, bubbles forming around laser-heated micro- and nanoparticles can serve as contrast agents in optoacoustic tomography.[11]

Since high temperatures and high pressures can be obtained around laser-irradiated microparticles, chemical reactions might also be triggered.[12] Therefore, knowledge of the particle's surface temperature required for bubble nucleation is essential to estimate whether photothermal damage (thermal disintegration of the particle itself or thermal denaturation of proteins in the vicinity of the particle) or photomechanical effects (bubbles) cause cell damage.[13–15]

In this paper, we focus on the bubble nucleation around absorbing microparticles, especially melanosomes, which are the main pigments of the RPE, to achieve a detailed understanding of microbubble formation in SRT. A few models of bubble dynamics around laser-heated melanosomes have been developed in the past with regard to laser safety considerations.[16–18] They improved understanding of laser-

Address all correspondence to Dr. Jörg Neumann, Medizinisches Laserzentrum Lübeck GmbH, Peter-Monnik-Weg 4, D-23562 Lübeck Germany.

1083-3668/2005/$22.00 © 2005 SPIE

induced retinal damage, but there is still a lack of experimental data to validate these models.

Therefore, the goal of this study is the experimental investigation of the nucleation temperature and threshold radiant exposures for bubble formation around melanosomes and other microbeads irradiated by nanosecond and microsecond laser pulses. The experimental bubble formation thresholds further enable the estimation of light absorption in RPE melanosomes.

## 2 Material and Methods

### 2.1 *Microparticles*

We use porcine retinal pigment epithelial melanosomes. Enucleated eyes are obtained from a local slaughterhouse. The eyes are dissected, the vitreous is removed, and purified water, which has been degassed and demineralized, is added. The neural retina is peeled off after a few minutes. Subsequently, the superficial RPE is removed by a stiff brush and purified by filter paper (Schleicher & Schüll 595 1/2, retention range 4 to 7 $\mu$m) to separate the melanosomes, which are released by expired cells, from cellular debris. As observed by light microscopy, porcine melanosomes are rotational ellipsoidal with mean diameters of $d_1 = d_2 = 0.8 \pm 0.1\,\mu$m and $d_3 = 2.3 \pm 0.6\,\mu$m.

Additionally, we used polyethylenimine-coated spherical gold beads with a diameter of 0.5 $\mu$m (MG-2/1, Chemicell GmbH, Germany) and spherical magnetic silica beads (SiMAG-EP, Chemicell GmbH, Germany), which contain 60% magnetite crystals ($<1\,\mu$m) embedded in a silica matrix. The surface of the SiMAG-EP beads is uncoated and contains hydrophilic silanol groups. The diameter of the SiMAG-EP particles is about 3 $\mu$m. SiMAG-EP and MG-2/1 beads were investigated to compare the results obtained for melanosomes to other particles.

The 25 $\mu$L of the aqueous microparticle suspension, which contains 0.1% agarose for immobilization of the particles, is given on an object slide for the experiments. The fluid reservoir is prevented from drying by using Gene Frames (Abgene, United Kingdom), which seal the reservoir and keep a distance of about 250 $\mu$m between the object slide and cover slip. Temperature-dependent measurements are performed in a cuvette with a depth of 4 mm, which enables us to adequately place the thermocouple of a digital thermometer (Lutron TM-914C, Type-K thermocouple). The cuvette can be heated electrically by a resistor and cooled by a peltier device.

### 2.2 *Experimental Setup*

The experimental setup for microparticle irradiation is shown in Fig. 1. The suspension, which contains microparticles, is observed by means of a video microscope using a standard 40× microscope objective. The microparticles are irradiated by a frequency-doubled *Q*-switched Nd:YAG (12 ns at 532 nm) and a Nd:YLF laser (527 nm), alternatively. The pulse duration of the modified Nd:YLF laser (Quantronix, Model 527DP-H) can be adjusted in the range of 200 ns to 5 $\mu$s by an active feedback system controlling the *Q*-switch.[19] The pulses are delivered by a fiber [Ceram Optec, Optron UV-A 105/125A/250, numerical aperture NA=0.22]. A top-hat beam profile at the specimen is achieved by imaging the fiber tip into the suspension. The fiber has a length of 200 m to

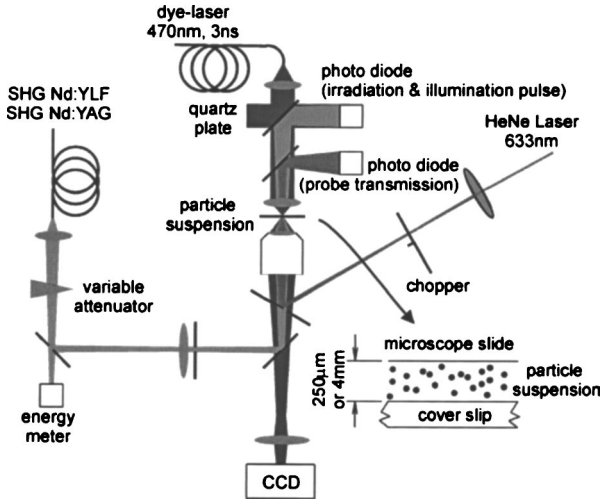


**Fig. 1** Experimental setup.

reduce spatial intensity modulation due to speckles below 15%. The circular irradiation spot has a diameter of 39.5 $\mu$m. A photodiode (Centronics, AEPX 65) with a current-integrating circuit is used to determine the pulse energy. The photodiode is calibrated by an energy meter (Ophir Optronics, Laserstar). The pulse energy is adjusted by a variable attenuator. A probe HeNe laser (Laser Graphics LK 8623, 632.8 nm) is coupled by a dichroic mirror into the optical path of the irradiation beam. The HeNe laser is chopped synchronized to the irradiation laser pulses with a duty cycle of 10 $\mu$s to 125 ms to avoid additional heating of the particles. The Gaussian radius of the probe beam is about 1.5 $\mu$m at the specimen. The probe transmission is detected in an open aperture geometry by a photodiode (EG&G, FND-100) and a 100-MHz current amplifier (femto, HCA-100M-50K-C). Fast flash photographs are taken by a CCD (JAI, CV-A11) and a frame grabber (National Instruments, IMAQ 1409). A $N_2$-pumped dye-laser (Laser Science, VSL-337-ND, DLM220) with a pulse duration of 3 ns serves as flash. Using the dye coumarin 102, the emission of the laser is tuned by an internal grating to 490 nm. The dye laser is triggered at an adjustable delay related to the irradiation pulse. The pulse energy of the dye laser at the particle suspension is below 1 $\mu$J per 200 $\mu$m-diam spot, resulting in a radiant exposure of less than 3 mJ/cm$^2$. Irradiation and illumination pulses are monitored by the same photodiode (Centronics, AEPX 65). Scattered light of the Nd:YLF/Nd:YAG laser is blocked by a short-pass filter in front of the CCD. The irradiation pulse shape; the illumination pulse shape; the irradiation pulse energy, which is taken from the calibrated photodiode; and the transmitted HeNe intensity are recorded by a digital oscilloscope (LeCroy, Waverunner LT374).

### 2.3 *Thermal Modeling*

Particle heating due to the absorbed laser radiation is modeled with the aid of Mathematica 4 (Wolfram Research, Inc.). The absorption efficiency $Q_{abs}$ of a spherical particle is given by the ratio of the absorption cross section $\sigma_{abs} = E_{abs}/H$ ($E_{abs}$, absorbed energy; $H$, radiant exposure) to the geometric cross section of the particle

**Table 1** Properties of the particles at T=20 °C.

| | $R_{model}$ ($\mu$m) | $\rho$ (kg/m$^3$) | $c_p$ (J/kg K) | $\kappa$ (m$^2$/s) | $R^2/4\kappa$ (ns) | $R^2/4\kappa_{H_2O}$ (ns) | $c_s$ (m/s) | $2R/c_s$ (ps) |
|---|---|---|---|---|---|---|---|---|
| Chemicell MG 2/1 (gold) | 0.25 | 19,300 | 130 | $1.23\times10^{-4}$ | 0.13 | 109 | 3390 | 140 |
| Chemicell SiMAG-EP | 1.5 | | | | | 3930 | | |
| silica | | 2200 | 800 | $4.6\times10^{-7}$ | 1200 | | 5900 | 500 |
| magnetite | | 5200 | 600 | $2.2\times10^{-6}$ | 260 | | 7100 | 420 |
| Melanosomes (melanin) | 0.5 | 1410 Ref. 41 | 2550 Ref. 44 | $1.4\times10^{-7}$ Ref. 45 | 450 | 437 | ~1500[a] | ~700 |
| Water | | 998 | 4180 | $1.43\times10^{-7}$ | | | 1482 | |

[a] Since the velocity of sound in melanin is not known, a typical value for polymers is used.

$$Q_{abs}=\sigma_{abs}/(\pi R^2),$$

where $R$ is the particle radius. The absorption efficiency $Q_{abs}=1.05$ of the spherical gold beads in water is calculated according to Mie theory[20] using the refractive index of gold in water [$m_{Au,H_2O}=0.59$ to $1.67i$ at $\lambda_{vac}=525$ nm (Ref. 20)] and a wavelength of $\lambda_{H_2O}=\lambda_{vac}/n_{H_2O}=395$ nm. Since a variation in the particle size, magnetite content and magnetite distribution in the silica matrix of the SiMAG-EP beads leads to significant differences in the optical properties of the individual particle, no modeling of the absorption of the SiMAG-EP beads was carried out. The absorption of RPE melanosomes is not well known and can be determined from the experiments by thermal modeling (Secs. 3.2 and 3.3). The heat equation

$$\frac{\partial T}{\partial t}-\kappa\nabla^2 T=\frac{A}{\rho c_p}, \tag{1}$$

where $T$ is temperature increase, $\kappa$ is thermal diffusivity, $\rho$ is density, $c_p$ is specific heat, $A$ is input power density (see Table 1) for a spherical particle, whose thermal properties differ from the surrounding medium, has been solved by Goldenberg and Tranter.[21] This solution

$$T_1(t,r)=R^2\frac{A}{K_1}\left[\frac{K_1}{3K_2}+\frac{1}{6}\left(1-\frac{r^2}{R^2}\right)-\frac{2Rb}{r\pi}\int_0^\infty\frac{(\sin y-y\cos y)\sin[(r/R)y]}{(c\sin y-y\cos y)^2+b^2y^2\sin^2 y}\times\frac{\exp[(-y^2/\gamma_1)t]}{y}\,dy\right]$$

$$T_2(t,r)=\frac{R^3}{r}\frac{A}{K_1}\left[\frac{K_1}{3K_2}-\frac{2}{\pi}\times\int_0^\infty\frac{(\sin y-y\cos y)[by\sin y\cos\sigma y-(c\sin y-y\cos y)\sin\sigma y]}{(c\sin y-y\cos y)^2+b^2y^2\sin^2 y}\times\frac{\exp[(-y^2/\gamma_1)t]}{y^3}\,dy\right] \tag{2}$$

$$b=\frac{K_2}{K_1}\left(\frac{\kappa_1}{\kappa_2}\right)^{1/2},\quad c=1-\frac{K_2}{K_1},\quad \sigma=\left(\frac{r}{R}-1\right)\left(\frac{\kappa_1}{\kappa_2}\right)^{1/2},$$

$$\gamma_1=\frac{R^2}{\kappa_1},$$

where $K=\kappa\rho c_p$ is thermal conductivity, was implemented in Mathematica. Properties of the medium inside the sphere are represented by the suffix 1, parameters of the surrounding are denoted by the suffix 2. Using the equation of state (EOS) of water according to International Association for Properties of Water and Steam (IAPWS-95) formulation[22] in the stable and data given by Skripov *et al.* in the metastable domain,[23] the isobaric volumetric heat capacity $\rho c_p$ for water at 0.1 MPa changes in the temperature range of 20 to 300 °C less than 10% relative to the value of $\rho c_p$ at 20 °C. Furthermore, the thermal conductivity of water $K$ according[24] to the IAPWS and its extrapolation in the metastable range was used to calculate the thermal diffusivity $\kappa=K/(\rho c_p)$. The relative variation of the thermal diffusivity $\kappa=K/(\rho c_p)$ in the temperature interval of 20 to 300 °C of water is less than 20%. Using the data given in Refs. 25 and 26, the relative change of the isobaric volumetric heat capacity and the thermal diffusivity of gold in the same temperature range are only 3 and 10%, respectively. Therefore, we assume for the calculations, that the thermal properties $\kappa$ and $\rho c_p$ including the properties of the melanosomes do not depend on the temperature.

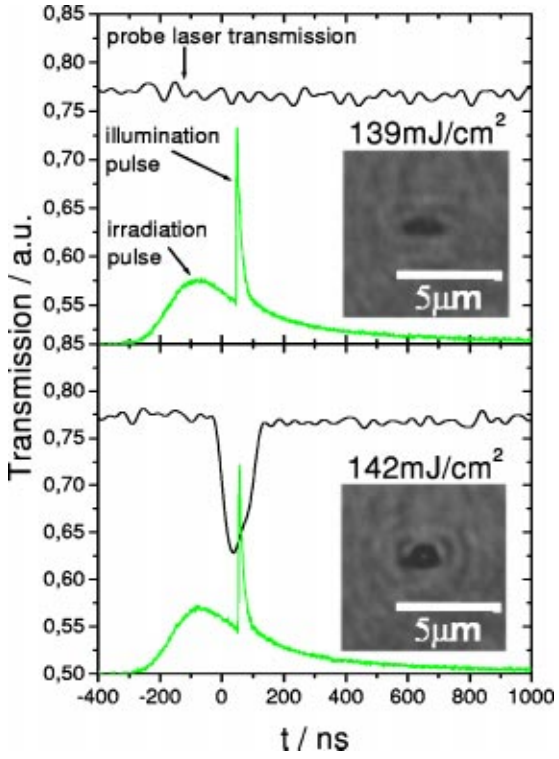


**Fig. 2** Probe laser transmission and fast flash photographs of the same melanosome below (139 mJ/cm$^2$) and above (142 mJ/cm$^2$) bubble threshold. The occurrence of a bubble on the photograph is accompanied by a transient decrease of the transmitted probe laser intensity. In addition, the irradiation pulse (240 ns) and the illumination (3 ns) pulse are plotted.

Since Goldenberg's solution assumes spatial and temporal homogenous heat deposition within the particle, the model was extended to arbitrary laser pulse shapes. Green's function, which is the temperature response for an infinitesimal short laser pulse, can be approximated at a given radius $r$ by

$$T_{\mathrm{Green}}(r,t) \approx T(r,t) - T(r,t-\Delta t), \qquad (3)$$

using a small time step $\Delta t$. A convolution of Green's function with the time-dependent power density of the absorbed light

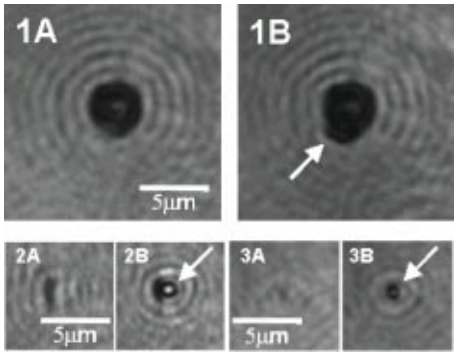


**Fig. 3** Typical fast flash photographs of a SiMAG-EP particle (1), a porcine RPE melanosome (2), and a MG-2/1 particle (3) taken before (a) and during bubble formation (b) at threshold radiant exposure. Irradiation pulse duration: (1b) 12 ns, (2b) 240 ns, and (3b) 12 ns. The particles are encircled by diffraction rings.

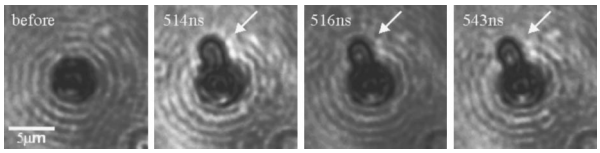


**Fig. 4** Bubble formation on a chemicell SiMAG-EP particle shows a reproducible nucleation site slight above threshold radiant exposure during consecutive irradiation ($\tau_{\mathrm{laser}}=1.8\ \mu$s, $H=970$ mJ/cm$^2$). The delay time relative to half the energy deposition can be found in the photographs.

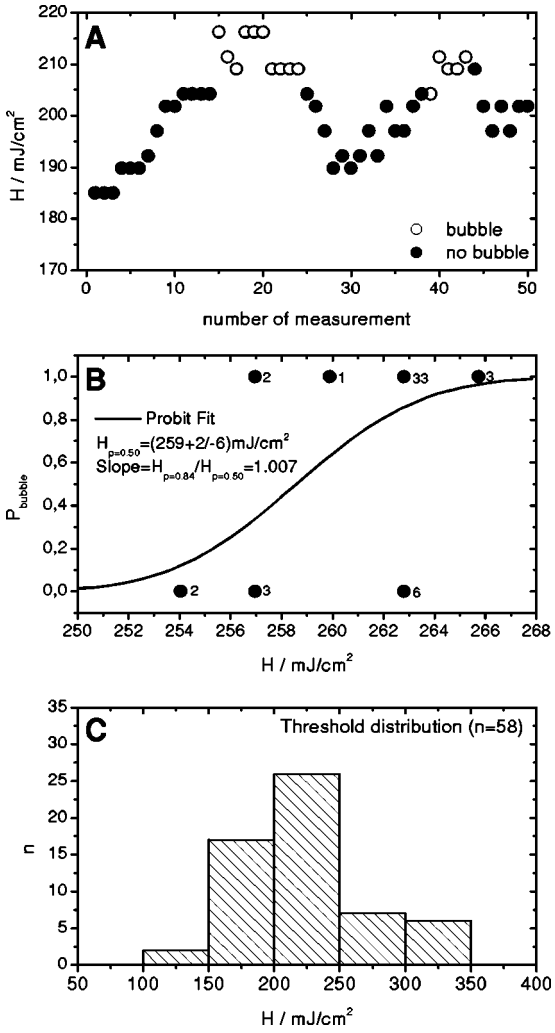


**Fig. 5** Melanosomes irradiated by 240-ns pulses: (a) no hysteresis of the bubble threshold can be observed during consecutive irradiation of the same melanosome, (b) probit fit for the bubble formation threshold of an individual melanosome, which is not the same melanosome as in (a). The numbers at the data points indicate the number of measurements, which are represented by the specific point. (c) Threshold distribution for bubble formation obtained from $n=58$ different melanosomes. This plot also shows, that the threshold radiant exposures for bubble formation measured for the two individual melanosomes in (a) ($H_s=205$ mJ/cm$^2$) and (b) ($H_s=259$ mJ/cm$^2$) are typical values.

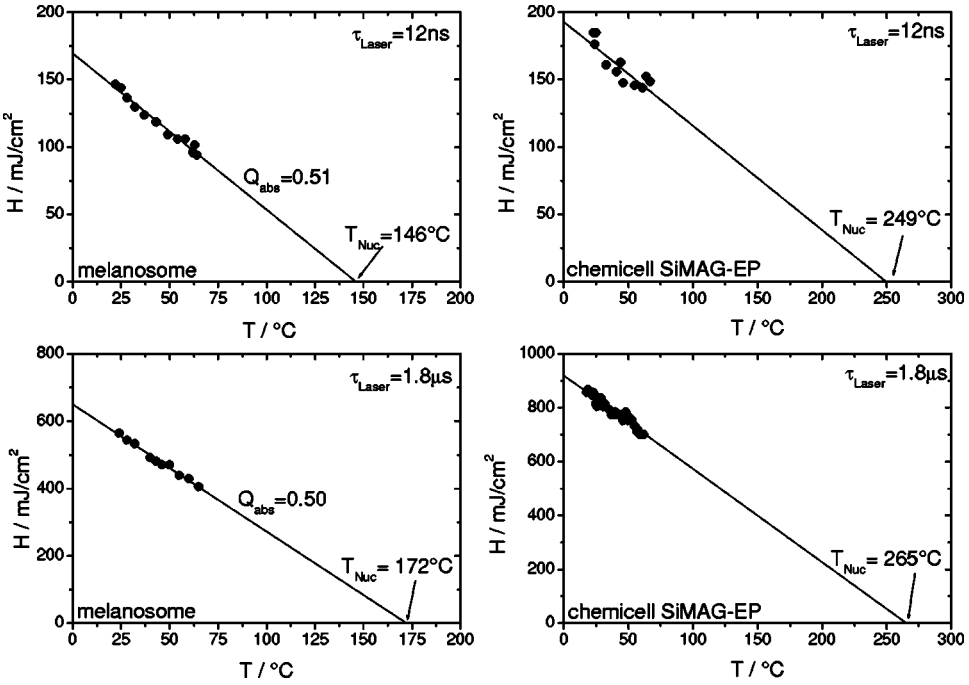


**Fig. 6** Temperature-dependent threshold measurements for individual melanosomes and chemicell SiMAG-EP beads irradiated by 12-ns and 1.8-$\mu$s pulses. The threshold for bubble formation decreases when the ambient temperature is increased, because less laser energy is required to reach the nucleation temperature $T_{\mathrm{nuc}}$. In addition, the absorption efficiency factor $Q_{\mathrm{abs}}$ of the melanosomes was calculated according to Eq. (6).

$$A(t)=I(t)\,\frac{Q_{\mathrm{abs}}\pi R^2}{(4/3)\,\pi R^3}, \tag{4}$$

where $I(t)$ is laser intensity, which is derived from the laser pulse shape, results in the temporal temperature course at a given radius $r$:

$$T(r,t)=T_{\mathrm{Green}}(r,t)\otimes A(t). \tag{5}$$

The condition of spatial homogeneous heat deposition within the particle is fulfilled, if the particle is optical thin ($1/\mu \gg R$, where $\mu$ is the absorption coefficient of the particle) or if the time of thermal relaxation is much smaller than the laser pulse duration ($R^2/4\kappa_1 \ll \tau_{\mathrm{laser}}$). Thermal parameters and the time of thermal relaxation of the particles can be found in Table 1.

## 3 Results

### 3.1 *Threshold for Bubble Formation*

Surface heating of the particle due to the probe HeNe laser is calculated to be below 10 °C for all particles in the first 5 $\mu$s after the HeNe is switched on. The bubble is usually probed in this time interval. The particles are irradiated with pulse durations of 12 ns, 240 ns, and 1.8 $\mu$s. Above a certain threshold of radiant exposure the probe transmission signals contain dips due to scattering of the HeNe light at the bubble. Coincidence from transmission measurements with the occurrence of bubbles is obtained by simultaneous fast flash photography (Fig. 2). The photographs reveal, that at threshold radiant exposure semispherical microbubbles form only on a part of the particle surface (Fig. 3). Photographs during consecutive irradiation taken at the same delay demonstrate, that the sites of nucleation on an individual particle are reproducible (Fig. 4). No hysteresis of the thresholds for bubble formation is found during repeated irradiation of the same particle near bubble threshold [Fig. 5(a)]. No morphological alterations of the particles have been observed by light microscopy after laser irradiation near threshold. The threshold for an individual particle at a fixed position towards the irradiation beam is very steep [Fig. 5(b)]. Fitting a probit distribution, typical slopes of $H_{p=0.84}/H_{p=0.50}<1.02$ are obtained for irradiation of the same particle, but there is a larger variation in the threshold radiant exposure between different particles of the same type [Fig. 5(c)].

### 3.2 *Temperature-Dependent Thresholds for Bubble Formation*

The nucleation temperature is obtained from temperature dependent threshold measurements for bubble formation. If the temperature of the particle suspension $T_{\mathrm{amb}}$ is increased, less absorbed radiant exposure $H_{\mathrm{thr}}$ is needed to reach the nucleation temperature $T_{\mathrm{nuc}}$ on the particle surface and cause bubble formation. Due to the linearity of the heat equation in $H$, the temperature increase on the particle surface per radiant exposure $\Delta T_{\mathrm{surf}}(H,Q_{\mathrm{abs}})/H$ is a constant, which depends for a given pulse shape and particle radius only on the absorption efficiency of the particle $Q_{\mathrm{abs}}$. The linear relationship

$$\begin{aligned} H_{\mathrm{thr}}(T_{\mathrm{amb}}) &= \frac{H}{\Delta T_{\mathrm{surf}}(H,Q_{\mathrm{abs}})}\,(T_{\mathrm{nuc}}-T_{\mathrm{amb}}) \\ &= B(Q_{\mathrm{abs}})(T_{\mathrm{nuc}}-T_{\mathrm{amb}}) \end{aligned} \tag{6}$$

can be extrapolated to the nucleation temperature, where no additional laser energy is needed to initiate vaporization.[27] We

**Table 2** Bubble nucleation temperatures $T_{nuc}$.

| $T_{nuc}$ | $\tau_{laser}=12$ ns | $\tau_{laser}=1.8\ \mu$s | $T_{mean}$ |
|---|---|---|---|
| Melanosomes | 136±23 °C | 157±33 °C | 147±20 °C |
| SiMAG-EP | 242±46 °C | 246±38 °C | 244±30 °C |

use a heating interval of 20 to 60 °C for $T_{amb}$ in the experiments. Particle motion due to thermal fluctuations prevent threshold measurements at higher temperatures. Figure 6 shows exemplary measurements of the nucleation temperature for individual particles. No hysteresis of the thresholds was observed during heating and cooling cycles. The mean nucleation temperatures are obtained from nucleation temperature measurements of $n=10$ individual particles for each particle type and each pulse duration (see Table 2). No reliable determination of the nucleation temperature was possible for the gold beads due to strong thermal motion of the particles at elevated temperatures and a small temperature dependence of the thresholds for bubble formation.

The nucleation temperature depends strongly on the particle species. The heating rates, which can be approximated by $(T_{nuc}-T_{amb})/\tau_{laser}$, are in the range of $10^8$ K/s for microsecond pulses and $10^{10}$ K/s for nanosecond pulses. No significant dependency of the nucleation temperature from the pulse duration is found. Therefore, the mean nucleation temperature $T_{mean}$ is averaged from the nucleation temperatures of the 12-ns and the 1.8-$\mu$s irradiation. Modeling the melanosome as a sphere with a radius of $R=0.5\ \mu$m, the efficiency factor of absorption $Q_{abs}$ can be determined from the slope of the temperature dependent bubble thresholds using the heat equation [Eq. (6)] (see Table 3).

### 3.3 *Thresholds for Bubble Formation versus Pulse Duration*

The mean threshold radiant exposures and corresponding standard deviations of $n>50$ different melanosomes and gold beads (Chemicell MG-2/1) are determined for each pulse duration (Fig. 7). Thresholds for the SiMAG-EP beads (magnetite/silica) are not determined due to a major variation in absorption (Sec. 2.3). Irradiation of the gold beads and the melanosomes with increasing pulse duration results in an increasing threshold radiant exposure for bubble formation due to heat conduction in the surrounding water during the laser pulse.

We use the thermal model from Sec. 2.3 to fit the experimental thresholds for bubble formation. In the model, the temperature on the particle surface is calculated as a function of the applied radiant exposure. The thermal model accounts for the laser pulse shape at each pulse duration. The model contains the absorption efficiency $Q_{abs}$ of the particles and the nucleation temperature $T_{nuc}$ as free parameters. For the gold beads, the absorption efficiency can be calculated according to Mie theory. Therefore, the nucleation temperature is the sole remaining fitting variable. For the melanosomes, the nucleation temperature has been determined experimentally (Sec. 3.2), which enables the calculation of the absorption efficiency.

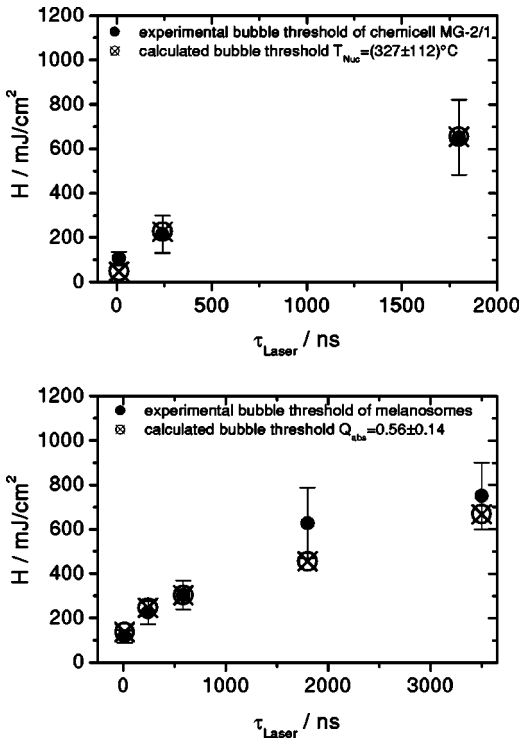


**Fig. 7** Experimental and calculated bubble formation thresholds of gold beads (chemicell MG-2/1) and melanosomes as a function of the pulse duration.

The nucleation temperature for the gold beads, which is obtained from the experimental bubble thresholds by a least-squares fit using the well-known optical and thermal properties of gold (Fig. 7, Table 1), is $T_{nuc}=327\pm112$ °C (for a 95% confidence interval).

Using a nucleation temperature of $T_{nuc}=150$ °C on the melanosome's surface, which is determined in Sec. 3.2, and a radius of $R=0.5\ \mu$m, the absorption efficiency of a melanosome $Q_{abs}$ is calculated by least square fitting. A value of $Q_{abs}=0.56\pm0.14$ (for a 95% confidence interval) is obtained.

### 3.4 *Onset of Bubble Formation*

The temporal onset of bubble formation is extracted from the transmitted intensity of the probe laser providing a temporal resolution of about 10 ns. This technique is sufficient to determine the point of bubble nucleation during the 240-ns and the 1.8-$\mu$s irradiation relative to the laser pulse. A few ($n>2$) individual particles were irradiated with increasing radiant exposure for each pulse duration. Since particles of the same type differ in their threshold for bubble formation [Fig. 5(c)], the applied radiant exposure for each particle is normalized to its bubble threshold irradiance $H_{thr}$ (Fig. 8). The tem-

**Table 3** Absorption efficiency $Q_{abs}$ of RPE melanosomes calculated from temperature dependent bubble thresholds.

| $Q_{abs}$ | $\tau_{laser}=12$ ns | $\tau_{laser}=1.8\ \mu$s | $Q_{abs,mean}$ |
|---|---|---|---|
| Melanosomes | 0.38±0.12 | 0.34±0.14 | 0.36±0.09 |

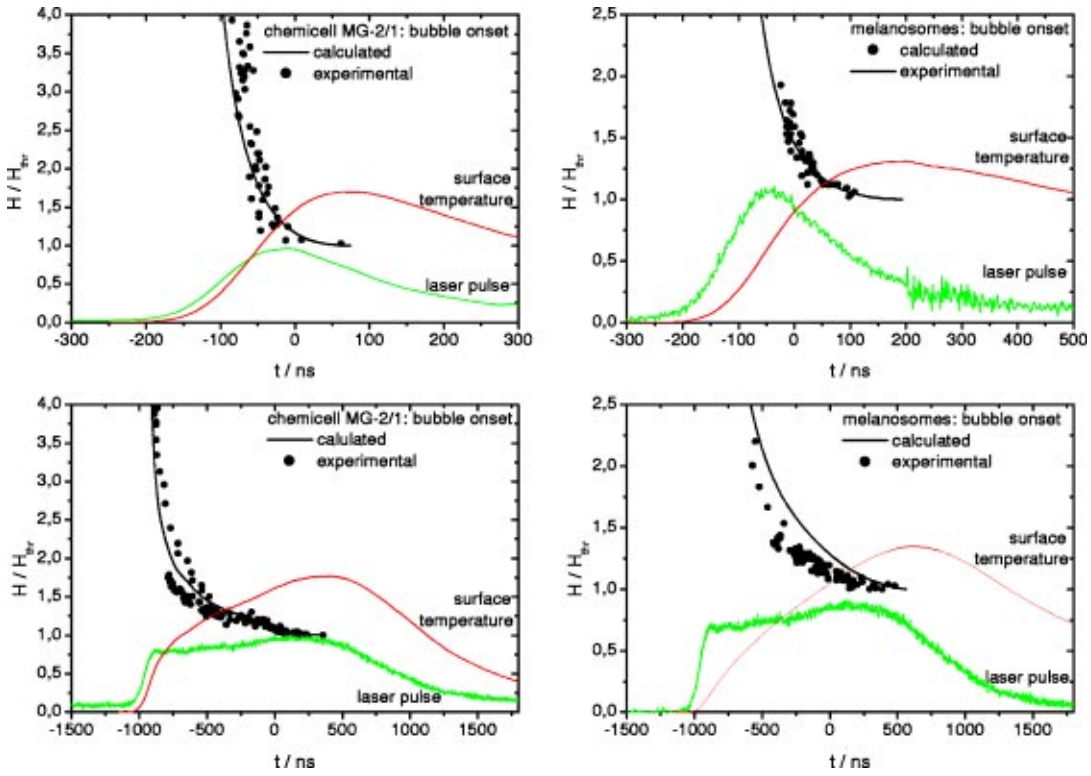


**Fig. 8** Experimental and calculated temporal bubble onset relative to the laser pulse as a function of the normalized radiant exposure. Due to larger heating rates, increasing radiant exposure leads to an earlier bubble onset. Additionally, the laser pulse and the calculated surface temperature of the particle are plotted in arbitrary units. (The temperature scales linearly with the radiant exposure.)

poral resolution obtained by the probe laser technique is not sufficient to resolve the bubble incipience relative to the laser pulse during the 12-ns irradiation. Therefore, we use fast flash images providing a temporal resolution of about 3 ns, which is given by the duration of the illumination pulse (Fig. 9). Due to larger heating rates, increasing radiant exposure leads to an earlier bubble onset at a constant nucleation temperature. The excess radiant exposure (expressed as a ratio $H/H_{\mathrm{thr}}$) required to nucleate a bubble at a time $t$ can be modeled due to the linearity of the heat equation in $H$ by

$$\frac{H(t)}{H_{\mathrm{thr}}} = \frac{\max_{\tau}[\Delta T_{\mathrm{surf}}(\tau, H_{\mathrm{thr}})]}{\Delta T_{\mathrm{surf}}(t, H_{\mathrm{thr}})}, \tag{7}$$

where $\Delta T_{\mathrm{surf}}(t, H_{\mathrm{thr}})$ is the surface temperature increase at time $t$ due to laser irradiation at threshold radiant exposure $H_{\mathrm{thr}}$. These calculated curves, which are depicted in Figs. 8 and 9, are in reasonable agreement with the experimental bubble incipience, which supports the thermal model. Particularly, the experimental bubble onset at threshold radiant exposure coincides in most cases with the point of time, where the maximum relative surface temperature is calculated. Small discrepancies between the experimental and the calculated bubble onset of the melanosomes might be explained by their ellipsoidal shape, which is unaccounted for in the thermal model.

## 4 Discussion

### 4.1 *Bubble Threshold*

Identical thresholds for bubble formation are obtained by probe laser transmission and photography (Fig. 2). The bubbles, which are observed at threshold have a diameter of about 0.7 $\mu$m, which is near the resolving power of our microscope (Fig. 2). These bubbles observed at threshold are

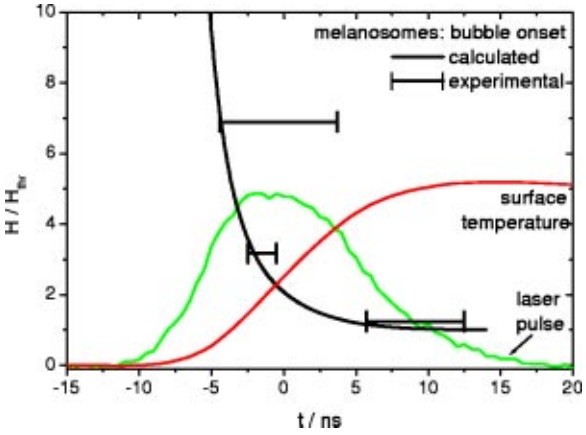


**Fig. 9** Calculated and experimental temporal bubble incipience relative to the 12-ns laser pulse. The laser pulse and the calculated surface temperature of the particle are plotted in arbitrary units.

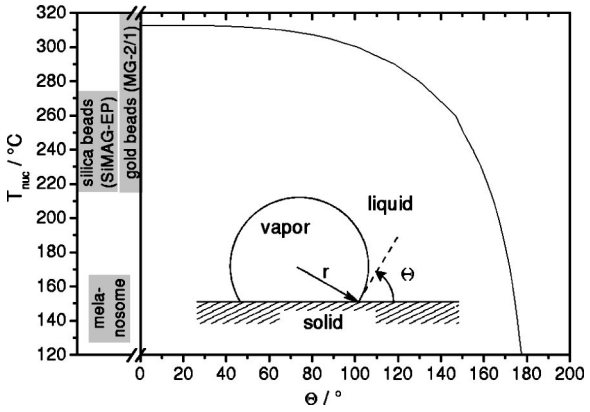


**Fig. 10** Heterogeneous nucleation temperature according to Eq. (9) as a function of the contact angle Θ. In addition, the experimental nucleation temperatures including the error intervals determined in Secs. 3.2 and 3.3 are plotted.

significantly smaller than in previously reported threshold measurements of isolated porcine RPE melanosomes, where a minimal bubble size of 2 $\mu$m has been resolved.[19] The enhanced spatial resolution reveals, that in most cases microbubbles form at threshold only on parts of the particle surface rather than around the whole particle like previously hypothesized.[19] Despite the enhanced resolving power of our experiments, our measured threshold radiant exposure values for porcine melanosomes are 40% higher than previously reported.[19] Although the threshold for a single particle is very steep [Fig. 5(b)], the deviation of bubble thresholds between individual particles of the same type [Fig. 5(c)] might be caused by differences in particle size (Sec. 4.5), surface topology (Sec. 4.2), and speckles during irradiation (Sec. 2.2). The melanosomes may also have a different melanin content depending on the stage of its maturation.[28]

### 4.2 *Nucleation Temperatures*

Since the applied pulses are much longer than the acoustic transit time of the particles $2R/c_s$ ($c_s$ is velocity of sound, see Table 1), only small thermoelastic pressure amplitudes are expected at threshold radiant exposure. Thus, the influence of tensile stress on the bubble nucleation is neglected in the further discussion. In most experiments on rapid transient heating, the nucleation temperature depends only weakly on the heating rate.[29,30] Such a weak dependence could not be observed in our measurements. Therefore, no significant difference has been found between the 12-ns and the 1.8-$\mu$s pulses in Sec. 3.2.

The temperature range, in which nucleation of water on heated surfaces can occur at atmospheric pressure, is restricted by the boiling point in thermodynamic equilibrium (100 °C) and the spinodal (~315 °C), where water becomes mechanically unstable.[31] Reviewing classical nucleation theory, there are different scenarios that lead to bubble nucleation on heated surfaces.[31]

#### 4.2.1 *Heterogeneous nucleation*

If no bubble nuclei preexist on the heated surface, bubbles can form only due to random statistical energy fluctuations on a molecular scale. If a bubble nucleus, which is produced by these thermodynamic fluctuations, grows beyond its critical radius, where the vapor pressure overcomes the ambient pressure and the surface tension, an observable bubble nucleates. For reasonable contact angles Θ between water and the solid (Fig. 10), the rate for heterogeneous nucleation on the particle surface is at the same temperature some orders of magnitude larger than the homogeneous nucleation rate in the surrounding fluid, which usually results in nucleation on the particle surface rather than in the surrounding fluid.[31] Since the fluid is heated by the particle, the highest fluid temperatures are obtained at the particle surface, which supports surface nucleation. Thus, we neglect the homogeneous nucleation rate in the following calculations. An approximation of the nucleation rate $J_{het}$ per surface area for heterogeneous nucleation is given in Ref. 31 by

$$J_{het}(T_l,\Theta)=\left[\frac{N_A\rho(T_l)}{M_{H_2O}}\right]^{2/3}\frac{1+\cos\Theta}{F(\Theta)}\left[\frac{3F(\Theta)\sigma(T_l)}{\pi\frac{M_{H_2O}}{N_A}}\right]^{1/2}\times\exp\left\{\frac{-16\pi F(\Theta)\sigma(T_l)^3}{3k_BT_l[\eta(T_l)p_{sat}(T_l)-p_l]^2}\right\},\tag{8}$$

$$F(\Theta)=\frac{1}{4}(1+\cos^2\Theta)(2-\cos\Theta),$$

$$\eta(T_l)=\exp\left[\frac{p_l-p_{sat}(T_l)}{\rho_l(T_l)R_{H_2O}T_l}\right],$$

where $T_l$ is the liquid temperature, $\rho(T)$ is the liquid density,[22] $p_l=1013$ hPa is the liquid pressure, $p_{sat}(T)$ is the saturated vapor pressure,[22] and $\sigma(T)$ is the surface tension.[32] Avogadro constant $N_A=6\times10^{26}$/kmol, molecular mass $M_{H_2O}=18$ kg/kmol, specific gas constant $R_{H_2O}=462$ J/kg K, and Boltzmann's constant $k_B=1.38\times10^{-23}$ J/K. Assuming a temperature course that follows the laser pulse, one obtains for the bubble threshold, which is defined by a probability of 50% for bubble formation

$$\int_0^{\tau_{laser}}J_{het}(T_{nuc},\Theta)4\pi R^2\mathrm{d}t=0.5.\tag{9}$$

The contact angle Θ as a function of the nucleation temperature $T_{nuc}$ according to Eq. (9) is plotted in Fig. 10. Pulse shape and duration as well as the different surface area of the particle types are negligible for this calculation. The nucleation temperature decreases with increasing contact angle. Nucleation temperatures near the spinodal, which are consistent with the nucleation temperature determined for gold beads, are obtained[31,33] for typical contact angles Θ in the range of $0\ \mathrm{deg}<\Theta<\Theta_{teflon}=108\ \mathrm{deg}$. The contact angles, which correspond to the nucleation temperatures determined in Sec. 3.2 (Fig. 10: $\Theta_{mel}(147\,°\mathrm{C})=175$ deg, $\Theta_{SiMAG\text{-}EP}(244\,°\mathrm{C})=153$ deg) suggest a quite nonwettable particle surface, which is extremely unlikely, for the surface of the magnetic

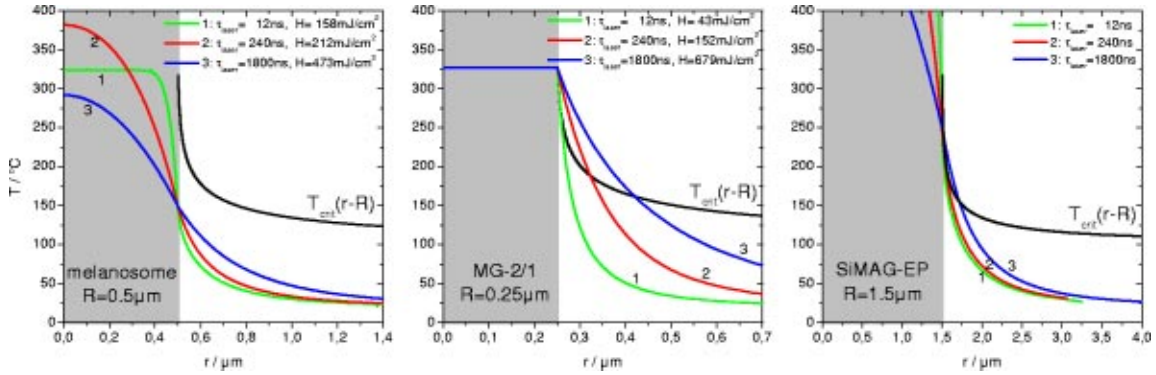


**Fig. 11** Hsu's criterion for inhomogeneous nucleation. The activation curve $T_{\mathrm{crit}}(r-R)$ for preexisting bubble nuclei with the radius $r-R$ must intersect the profile of the maximum temperature $\max_t[T(t,r)]$ around the particle to activate the bubble nuclei [see Eq. (11)]. For irradiation, a temporal flat top pulse was assumed. (The thermal properties of silica and a surface temperature at the end of the pulse of 250 °C are assumed for the SiMAG-EP beads.) Inhomogeneous nucleation is possible for SiMAG-EP (magnetite/silica) and MG-2/1 (gold) beads, but not for the melanosomes.

silica particles (SiMAG-EP) contains hydrophilic silanol groups. Moreover, the photographs of transient bubbles on the particle surface (e.g., Fig. 4) are not consistent with contact angles $\Theta \gg 100$ deg. It is more likely that other mechanisms lead to bubble nucleation on SiMAG-EP beads and melanosomes.

### 4.2.2 *Inhomogeneous nucleation*

Gas or steam can be entrapped in crevices on the particle surface.[34] Due to heating, the vapor pressure in the crevice increases and can overcome surface tension, which leads to bubble growth. The critical radius of a steam bubble is given by[31]

$$r_{\mathrm{crit}}(T_l) = \frac{2\sigma(T_l)}{\eta(T_l)p_{\mathrm{sat}}(T_l) - p_l}. \tag{10}$$

Bubbles smaller than the $r_{\mathrm{crit}}$ will collapse due to insufficient vapor pressure, while bubbles larger than $r_{\mathrm{crit}}$ will grow spontaneously. Thus, the nucleation temperature depends mainly on the size of the preexisting nucleus. Assuming pure steam in the crevice, the size of active nucleation cavities can be estimated by Hsu's criterion for nucleate boiling on heated surfaces in nonuniform temperature fields.[35] According to Hsu, inhomogeneous nucleation takes place if a preexisting steam bubble radius with the radius $r$ becomes critical within the thermal boundary layer of the heated surface. Thus, for the bubble the condition

$$T_{\mathrm{crit}}(r) < \max_t[T_2(t, R+r)] \tag{11}$$

must be satisfied to overcome ambient pressure and surface tension. $T_{\mathrm{crit}}(r)$ is the temperature of a bubble, which is critical at a radius of $r$, [inverse of Eq. (10); for $T_2(r,t)$, see Eq. (2)]. The plots of the activation curve and the temperature in the surrounding fluid show, that nucleation on SiMAG-EP particles by this mechanism is very likely (Fig. 11). Nucleation by steam or gas cavities often corresponds to reproducible nucleation sites, which were observed during repeated irradiation above threshold for bubble formation (Fig. 4). Also the nucleation on gold particles is consistent with Hsu's criterion. [The nucleation temperature is often estimated by Eq. (10) using the particle radius as critical radius $r_{\mathrm{crit}}$. This implies, that the whole particle acts as nucleation center, which is not supported by Figs. 2, 3, and 4. The assumption, that the whole particle is the nucleation center, is equivalent to an unrealistic contact angle of 180 deg and gives, therefore, only the lower limit of the nucleation temperature.]

A comparison to nucleation experiments on film heaters,[30] which are used in bubble jet technology, or thin wires,[29] show that an electrical heating duration in the microsecond range results on metallic surfaces in nucleation temperatures in the range of 270 to 300 °C. On silica surfaces a nucleation temperature of 250 °C was found during pulsed laser heating.[36] These temperatures are similar to the nucleation temperatures we have measured for gold and magnetic silica beads.

The nucleation temperature of melanosomes is significantly lower and cannot solely be explained by steam crevices, because the thermal boundary layer is too small to activate preexisting bubble nuclei on the surface (Fig. 11). In contrast to the chemically inert materials of the inorganic microbeads, a chemical reaction of melanin, which produces gas, or vaporization of hydratation water in the melanosome, cannot be excluded by the experiments and might support bubble formation at lower temperatures. Glickman et al.[37] found morphological damage on the surface of bovine RPE melanosomes, which induces oxidative stress, by scanning electron microscopy (SEM) after multiple irradiation by a 10-ns laser pulse at 214 mJ/cm$^2$ ($y = \lambda 532$ nm). Glickman *et al.* hypothesized that vaporization of the melanosome's hydratation water, which is released during continuous heating in a temperature range of 100 to 130 °C (Ref. 38), causes this kind of damage. Furthermore, Piattelli and Nicolaus[39] have observed thermal decarboxylation of melanin, which results in a release of $CO_2$ during heating of melanin to 140 to 150 °C. On the other hand, Hayes and Wolbarsht have found no morphologic changes of dog RPE melanosomes by SEM after heating them in standard atmosphere to 350 °C. Since we do not observe any threshold hysteresis or residual bubbles after transient bubble formation [Fig. 5(a)], only a small amount of noncondensable gas can be produced within the melanosome, whereas irradiation a few times above threshold leads to

**Table 4** Calculated absorption coefficients of RPE melanosomes.

| | $Q_{abs,T_{nuc}}=0.36\pm0.09$ | $Q_{abs,\tau}=0.56\pm0.14$ | $Q_{abs,mean}=0.46$ |
|---|---|---|---|
| $\mu$ ($\mu m^{-1}$) | 0.54±0.14 | 0.83±0.22 | 0.69 |

stable bubbles of noncondensable gas, which is usually explained by thermal disintegration of the melanosome.[40]

### 4.3 *Onset of Bubble Formation*

A comparison of the experimental and the calculated bubble onset shows a good agreement, which supports our thermal model of the heated particles (Figs. 8 and 9). The bubble nucleates during the laser pulse even for nanosecond pulses (Fig. 9). In some models on bubble formation around laser heated melanosomes, nucleation takes place after the laser pulse.[18] As no evidence for a delayed phase transition was found, our experiments do not support this hypothesis.

### 4.4 *Absorption Coefficient of RPE Melanosomes*

The mean absorption efficiency $Q_{abs}$ obtained by temperature dependent ($Q_{abs,T_{nuc}}$) and by pulse duration dependent ($Q_{abs,\tau}$) bubble thresholds differ. In principle, both techniques should lead to the same absorption efficiency values. A reason for the differences between $Q_{abs,T_{nuc}}$ and $Q_{abs,\tau}$ was not found. However, the error bars obtained for both absorption efficiencies overlap. To compare the measured absorption efficiency of RPE melanosomes to absorption coefficients reported by other authors, we neglect the effects of Mie scattering and calculate the internal absorption coefficient of a RPE melanosome according to Gerstman et al.[16] by geometric optics and Beer's law. Using the first-order series approximation in $\mu$R, which corresponds to optical thin particles (homogeneous deposition of the absorbed energy) one obtains

$$Q_{abs}=\frac{E_{abs}}{H\pi R^2}\approx\frac{4}{3}\ (\mu R). \tag{12}$$

**Table 5** Absorption coefficients of RPE melanosomes from previous studies.

| | $\mu$ ($\mu m^{-1}$) |
|---|---|
| Glickman et al.,[41] bovine (532 nm) | 0.23 |
| Williams et al.,[42] mouse (~530 nm) | 0.9–1.1 |
| Brinkmann et al.,[19] porcine (527/532 nm) | 0.8 |
| Strauss et al.,[43] bovine (532 nm) | 0.6–0.8 |

The resulting homogeneous absorption coefficients are listed in Table 4. These calculated absorption coefficients are in reasonable agreement with absorption coefficients of RPE melanosomes, which have been found in previous studies (see Table 5).

### 4.5 *Calculated Threshold Dependence on the Particle Size*

Using the experimental homogeneous absorption coefficient of $\mu=0.7\ \mu m^{-1}$ for melanosomes, the surface temperature as a function of the melanosome size is calculated and compared to the calculated surface temperature of gold beads (Fig. 12). The absorption of the melanosomes is approximated by Eq. (12), whereas the absorption of gold particles is determined according to Mie theory. In Fig. 12, we choose radiant exposure values for the calculations, which lead for melanosomes at $R=0.5\ \mu m$ to the nucleation temperature of $T_{nuc}=150\,°C$ and for gold beads at $R=0.25\ \mu m$ to $T_{nuc}=300\,°C$, respectively. Since melanosomes are optically thin, the energy is absorbed homogeneously within the volume resulting in a temperature increase, which does not depend on the particle size (12-ns laser pulse duration). But if the particle size becomes smaller, the condition of thermal confinement $\tau_{laser} \ll R^2/(4\kappa_{H_2O})$ (see Table 1) is not fulfilled for long pulses (240 ns and 1.8 $\mu$s) and appreciable heat diffusion during the pulse leads to less effective melanosome heating. Growing

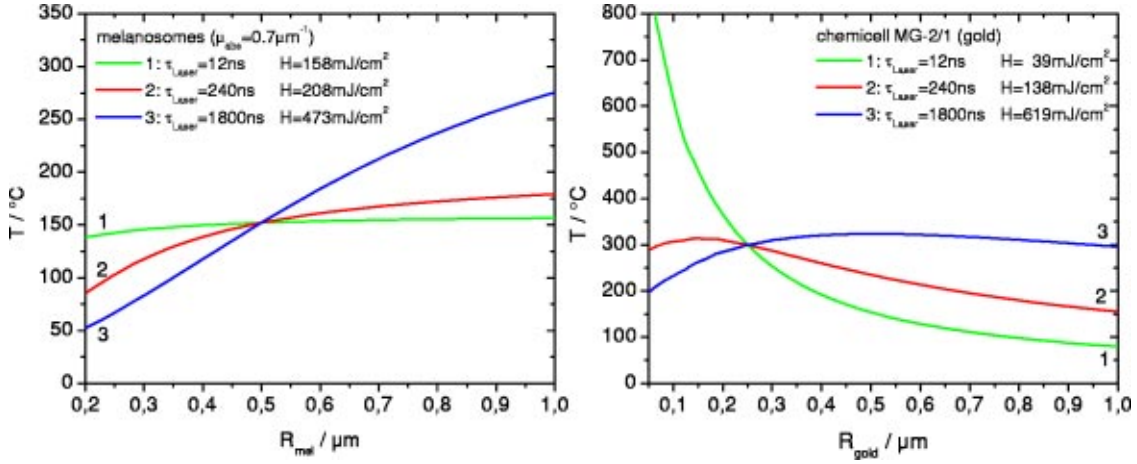


**Fig. 12** Calculated temperature on the particle surface as a function of the particle radius at the end of a temporal flat top laser pulse of constant radiant exposure. We choose radiant exposure values, which lead for melanosomes at $R=0.5\ \mu m$ to the nucleation temperature of $T_{nuc}=150\,°C$ and for the gold beads at $R=0.25\ \mu m$ to $T_{nuc}=300\,°C$.

particle size of the gold beads, which are optically thick ($Q_{abs} \approx 1$, if the surface reflectivity is neglected) leads to a decreasing density of the absorbed energy

$$\frac{E_{abs}}{V} = \frac{Q_{abs} \pi R^2 H}{(4/3)\pi R^3} \propto \frac{1}{R}, \tag{13}$$

which can be observed in Fig. 12 for the 12-ns pulse duration, because in the thermal confinement the temperature increase is proportional to the absorbed energy density at constant radiant exposure. Again, the particle heating becomes less effective for long pulses (240 ns and 1.8 $\mu$s) and small particle sizes due to appreciable heat conduction in the surrounding water during the laser pulse.

## 5 Conclusion

The nucleation of bubbles on laser-heated microparticles was investigated. It was demonstrated by flash photography, that the whole particle does not act as the nucleation center, but the bubbles nucleate heterogeneously on the particle's surface. The thresholds for bubble nucleation on melanosomes were determined for pulse durations in the nanosecond and microsecond range. A mean absorption efficiency of $Q_{abs} = 0.46$ was calculated by thermal modeling of bubble formation thresholds as a function of temperature and pulse duration. The nucleation temperature of bubbles on a melanosome, which is extrapolated from temperature dependent bubble thresholds, is $T_{nuc} = 147 \pm 20\,^{\circ}\mathrm{C}$. For inorganic silica magnetite beads and gold beads, nucleation temperatures of $T_{nuc} = 244 \pm 30\,^{\circ}\mathrm{C}$ and $T_{nuc} = 327 \pm 112\,^{\circ}\mathrm{C}$ are found, which are significantly higher than for melanosomes. The bubble incipience relative to the irradiation pulse was studied and was found to be in good agreement with thermal modeling. It was shown that the bubbles can nucleate for all applied pulse durations, including for 12 ns pulses, during the pulse.

### *Acknowledgments*

We are grateful to Dr. Gereon Hüttmann for making his self-written Mathematica library on heat diffusion and Mie scattering available to us. We also thank Chemicell GmbH, Berlin, Germany, for providing us with microbeads. One of the authors (J.N.) is supported by a fellowship of the FAZIT-Stiftung, Frankfurt am Main, Germany.

### *References*

1. R. R. Anderson and J. A. Parrish, ''Selective photothermolysis: precise microsurgery by selective absorption of pulsed radiation,'' *Science* **220**, 524–527 (1983).
2. B. S. Gerstman, ''Nanosecond laser pulses: from retinal damage to refined surgical treatment of congenital nevi and melanoma,'' in *Laser-Tissue Interaction VIII*, *Proc. SPIE* **2975**, 180–191 (1997).
3. J. Roider, R. Brinkmann, C. Wirbelauer, H. Laqua, and R. Birngruber, ''Retinal sparing by selective retinal pigment epithelial photocoagulation,'' *Arch. Ophthalmol. (Chicago)* **117**, 1028–1034 (1999).
4. J. Roider, R. Brinkmann, C. Wirbelauer, H. Laqua, and R. Birngruber, ''Subthreshold (retinal pigment epithelium) photocoagulation in macular diseases: a pilot study,'' *Br. J. Ophthamol.* **84**, 40–47 (2000).
5. J. Roider, F. Hillenkamp, T. Flotte, and R. Birngruber, ''Microphotocoagulation: selective effects of repetitive short laser pulses,'' *Proc. Natl. Acad. Sci. U.S.A.* **90**, 8643–8647 (1993).
6. J. Roider, E. El Hifnawi, and R. Birngruber, ''Bubble formation as primary interaction mechanism in retinal laser exposure with 200 ns laser pulses,'' *Lasers Surg. Med.* **22**, 240–248 (1998).
7. C. P. Lin, M. W. Kelly, S. A. B. Sibayan, M. A. Latina, and R. R. Anderson, ''Selective cell killing by microparticle absorption of pulsed laser irradiation,'' *IEEE J. Sel. Top. Quantum Electron.* **5**, 963–968 (1999).
8. D. Leszczynski, C. M. Pitsillides, R. K. Pastila, R. R. Anderson, and C. P. Lin, ''Laser-beam-triggered microcavitation: a novel method for selective cell destruction,'' *Radiat. Res.* **156**, 399–407 (2001).
9. C. M. Pitsillides, E. K. Joe, X. Wei, R. R. Anderson, and C. P. Lin, ''Selective cell targeting with light-absorbing microparticles and nanoparticles,'' *Biophys. J.* **84**, 4023–4032 (2003).
10. V. P. Zharov, V. Galitovsky, and M. Viegas, ''Photothermal detection of local thermal effects during selective nanophotothermolysis,'' *Appl. Phys. Lett.* **83**, 4897–4899 (2003).
11. A. A. Karabutov, E. V. Savateeva, and A. A. Oraevsky, ''Optoacoustic supercontrast for early cancer detection,'' in *Biomedical Optoacoustics II*, *Proc. SPIE* **4256**, 179–187 (2001).
12. T. E. McGrath, G. J. Diebold, D. M. Bartels, and R. A. Crowell, ''Laser-initiated chemical reactions in carbon suspensions,'' *J. Phys. Chem. A* **106**, 10072–10078 (2002).
13. G. Hüttmann and R. Birngruber, ''On the possibility of high-precision photothermal microeffects and the measurement of fast thermal denaturation of proteins,'' *IEEE J. Sel. Top. Quantum Electron.* **5**, 954–962 (1999).
14. G. Hüttmann, J. Serbin, B. Radt, B. I. Lange, and R. Birngruber, ''Model system for investigating laser-induced subcellular microeffects,'' in *Laser-Tissue Interaction XII*, *Proc. SPIE* **4257**, 398–409 (2001).
15. G. Hüttmann, B. Radt, J. Serbin, and R. Birngruber, ''Inactivation of proteins by irradiation of gold nanoparticles with nano- and picosecond laser pulses,'' in *Therapeutic Laser Applications and Laser-Tissue Interactions*, *Proc. SPIE* **5142**, 88–95 (2003).
16. B. S. Gerstman, C. R. Thompson, S. L. Jacques, and M. E. Rogers, ''Laser induced bubble formation in the retina,'' *Lasers Surg. Med.* **18**, 10–21 (1996).
17. J. M. Sun, B. S. Gerstman, and B. Li, ''Bubble dynamics and shock waves generated by laser absorption of a photoacoustic sphere,'' *J. Appl. Phys.* **88**, 2352–2362 (2000).
18. V. K. Pustovalov, ''Thermal processes under the action of laser radiation pulse on absorbing granules in heterogeneous biotissues,'' *Int. J. Heat Mass Transfer* **36**, 391–399 (1993).
19. R. Brinkmann, G. Hüttmann, J. Rögener, J. Roider, R. Birngruber, and C. P. Lin, ''Origin of retinal pigment epithelium cell damage by pulsed laser irradiance in the nanosecond to microsecond time regimen,'' *Lasers Surg. Med.* **27**, 451–464 (2000).
20. H. C. van de Hulst, *Light Scattering by Small Particles*, Dover, New York (1981).
21. H. Goldenberg and C. J. Tranter, ''Heat flow in an infinite medium heated by a sphere,'' *Br. J. Appl. Phys.* **3**, 296–298 (1952).
22. The International Association for Properties of Water and Steam (IAPWS), *The IAPWS Formulation 1995 for the Thermodynamic Properties of Ordinary Water Substance for General and Scientific Use*, available at www.iapws.org (1995).
23. V. P. Skripov, E. N. Sinitsyn, P. A. Pavlov, G. V. Ermakov, G. N. Muratov, N. V. Bulanov, and V. G. Baidakov, *Thermophysical Properties of Liquids in the Metastable (Superheated) State*, Gordon and Breach Science Publishers, New York (1988).
24. The International Association for Properties of Water and Steam (IAPWS), *Revised Release on the IAPS Formulation 1985 for the Thermal Conductivity of Ordinary Water Substance*, available at www.iapws.org (1998).
25. O. L. Anderson, D. G. Isaak, and S. Yamamoto, ''Anharmonicity and the equation of state for gold,'' *J. Appl. Phys.* **65**, 1534–1543 (1989).
26. D. R. Lide, Ed., *CRC Handbook of Chemistry and Physics*, 76th ed., CRC Press, Boca Raton, FL (1995).
27. S. L. Jacques and D. J. McAuliffe, ''The melanosome: threshold temperature for explosive vaporization and internal absorption coefficient during pulsed laser irradiation,'' *Photochem. Photobiol.* **53**, 769–775 (1991).
28. M. Boulton, ''Melanin and the retinal pigment epithelium,'' in *The Retinal Pigment Epithelium*, M. F. Marmor and T. J. Wolfensberger, Eds., pp. 68–85, Oxford University Press, New York (1998).
29. S. Glod, D. Poulikakos, Z. Zhao, and G. Yadigaroglu, ''An investigation of microscale explosive vaporization of water on an ultrathin pt wire,'' *Int. J. Heat Mass Transfer* **45**, 367–379 (2002).
30. Y. Iida, K. Okuyama, and K. Sakurai, ''Boiling nucleation on a very

small film heater subjected to extremely rapid heating,'' *Int. J. Heat Mass Transfer* **37**, 2771–2780 (1994).
31. V. P. Carey, *Liquid-Vapor Phase Change Phenomena*, Hemisphere Publishing Corporation, Washington (1992).
32. The International Association for Properties of Water and Steam (IAPWS), *IAPWS Release on Surface Tension of Ordinary Water Substance*, available at www.iapws.org (1994).
33. A. W. Adamson and A. P. Gast, *Physical Chemistry of Surfaces*, 6th ed., Wiley-Interscience, New York (1997).
34. M. Holmberg, A. Kühle, J. Garnaes, K. A. Morch, and A. Boisen, ''Nanobubble trouble on gold surfaces,'' *Langmuir* **19**, 10510–10513 (2003).
35. Y. Y. Hsu, ''On the size range of active nucleation cavities on a heating surface,'' *J. Heat Transfer* **84**, 207–216 (1962).
36. T. Brendel and R. Brinkmann, ''Mid-IR laser induced superheating of water and its quantification by an optical temperature probe,'' *Appl. Opt.* **43**, 1856–1862 (2004).
37. R. D. Glickman, S. L. Jacques, J. A. Schwartz, T. Rodriguez, K.-W. Lam, and G. Buhr, ''Photodisruption increases free radical reactivity of melanosomes isolated from retinal pigment epithelium,'' in *Laser-Tissue Interaction VII*, *Proc. SPIE* **2681**, 460–467 (1996).
38. P. Baraldi, R. Capelletti, P. R. Crippa, and N. Romeo, ''Electrical characteristics and electret behavior of melanin,'' *J. Electrochem. Soc.* **126**, 1207–1212 (1979).
39. M. Piattelli and R. A. Nicolaus, ''The structure of melanins and melanogenesis I,'' *Tetrahedron* **15**, 66–75 (1961).
40. J. Neumann and R. Brinkmann, ''Microbubble dynamics around melanosomes irradiated with microsecond pulses,'' in *Laser-Tissue Interactions XIII*, *Proc. SPIE* **4617**, 180–186 (2002).
41. R. D. Glickman, S. L. Jacques, R. T. Hall, and N. Kumar, ''Revisiting the internal absorption coefficient of the retinal pigment epithelium melanosome,'' in *Laser-Tissue Interaction XII*, *Proc. SPIE* **4257**, 134–141 (2001).
42. M. A. Williams, L. H. Pinto, and J. Gherson, ''The retinal pigment epithelium of wild type (C57BL/6J +/+) and pearl mutant (C57BL/6J pe/pe) mice,'' *Invest. Ophthalmol. Visual Sci.* **26**, 657–669 (1985).
43. M. Strauss, P. A. Amendt, R. A. London, D. J. Maitland, M. E. Glinsky, C. P. Lin, and M. W. Kelly, ''Computational modeling of stress transients and bubble evolution in short pulse laser irradiated melanosome particles,'' in *Laser-Tissue Interaction VIII*, *Proc. SPIE* **2975**, 261–270 (1997).
44. J. R. Hayes and M. L. Wolbarsht, ''Thermal model for retinal damage induced by pulsed lasers,'' *Aerosp. Med.* **39**, 474–480 (1968).
45. I. A. Vitkin, J. Woolsley, B. C. Wilson, and R. R. Anderson, ''Optical and thermal characterization of natural melanin,'' *Photochem. Photobiol.* **59**, 455–462 (1994).